Inorg. Chem. **2008**, *47*, 468–480

Syntheses, Crystal Structures, and Spectral Properties of a Series of 3,8-Bisphenyl-1,10-phenanthroline Derivatives: Precursors of 3,8-Bis(4-mercaptophenyl)-1,10-phenanthroline and Its Ruthenium(II) Complex for Preparing Nanocomposite Junctions with Gold Nanoparticles between 1 μm Gap Gold Electrodes

Wei Huang,*[,†,‡] Gou Masuda,[||] Seisuke Maeda,[||] Hirofumi Tanaka,[†,§] Takami Hino,[†] and Takuji Ogawa*[,†,§]

Research Center for Molecular-Scale Nanoscience, Institute for Molecular Science, 5-1 Higashiyama, Myodaiji, Okazaki 444-8787, Japan, State Key Laboratory of Coordination Chemistry, Coordination Chemistry Institute, Nanjing University-Jinchuan Group Ltd. Joint Laboratory of Metal Chemistry, School of Chemistry and Chemical Engineering, Nanjing University, Nanjing 210093, China, Department of Chemistry, Faculty of Science, Ehime University, Bunkyo-cho 2-5, Matsuyama, Ehime 790-8577, Japan, Core Research for Evolutional Science and Technology (CREST) of Japan Science and Technology Agency (JST), Hon-machi 4-1-8, Kawaguchi, Saitama, 332-0012, Japan

Received July 1, 2007

A multistep synthesis was achieved to obtain 3,8-bis(4-mercaptophenyl)-1,10-phenanthroline, which has two free thiol end groups with a molecular length of 1.89 nm, and its ruthenium(II) complex. Five single-crystal structures and UV–vis spectra of related intermediates in methanol and the solid state were studied in order to obtain additional information on the molecules as well as on the supramolecular interactions in the structures. Thermal and electrochemical properties of related Ru(II) complexes were also involved. 3,8-Bis(4-mercaptophenyl)-1,10-phenanthroline and one of its ruthenium(II) complexes were then treated with gold nanoparticles (Au-NPs) via in situ thiol-to-thiol ligand exchange in the presence of two facing Au electrodes with a 1×1 μm^2 gap. Stable molecular junctions composed of self-assembled films were produced as revealed by an obvious increase of the conductivity between the Au electrodes, wherein dithiols-bridged Au-NPs were attached to the electrodes by means of Au–S-bonded contacts. Temperature-dependent current–voltage (I–V) measurements for the junctions were performed in the temperature range of 7–300 K, and classical Arrhenius plots and their linear fits were obtained to determine the average activation energies (ΔE) of these devices. It is found that when the Ru(II) ion is introduced, the conductivity of the nanodevice is increased and the energy barrier is lowered under the same experimental conditions.

1. Introduction

Organic molecular electronic devices have been suggested to be the next generation of electronic devices.[1] Compared to inorganic semiconductors, formation of chemical bonds between atoms has reduced dimensionality in organic molecules where interactions within the molecular chain are much stronger than those between neighboring chains, which makes these systems more susceptible to structural distortions.[2,3] Thus, it is crucial to rationally design and synthesize organic molecules, especially for those having conjugated π systems since the structures of the molecules will dominate the properties of organic molecular electronic devices.

Self-assembly is an inherently manufacturable process that is technically attractive and cost effective since a self-assembled system attempts to reach a thermodynamically stable state driven by global minimization of free energy.[4,5] Meanwhile, nanoparticles can serve as building blocks or templates for fabricating functional nanostructures and mo-

* To whom correspondence should be addressed. Email: whuang@nju.edu.cn (W.H.); ogawat@ims.ac.jp (T.O.).
† Institute for Molecular Science.
‡ Nanjing University.
|| Ehime University.
§ Core Research for Evolutional Science and Technology of Japan Science and Technology Agency.

10.1021/ic701295q CCC: $40.75
Published on Web 12/15/2007

lecular-based electronic devices via a so-called bottom-up approach.[6] For example, Au-NPs can combine with a variety of thiol-group-ended molecules or terminal thiol-modified surfaces by means of a covalent gold−sulfur bond to form self-assembled clusters,[7] monolayers,[8] and multilayers.[9]

Following the idea of combining specific organic dithiol end-capped molecules and certain nanoparticles via a self-assembly method to fabricate nanodevices,[10] we have been engaging in synthesizing π-conjugated molecules that have dithiol groups at both ends as the connecting parts for gap gold electrodes and investigating the electrical and/or optical properties of these nanodevices. For example, a series of oligothiophene dithiols with 3, 6, and 9 thiophene rings in the molecules was first utilized in combination with active Au-NPs bridging 1 μm gap Au electrodes via strong Au−S contacts.[11] The resulting self-assembled thin films exhibited reproducible temperature-dependent $I-V$ characteristics and photoresponsive properties.

To further explore our investigations, 3,8-bis(4-mercaptophenyl)-1,10-phenanthroline (**10**) and its transition-metal complexes were selected as the target molecules with the aim of evaluating the effects of introducing metal ions into the system and realizing highly functional molecular devices. In this paper, we report (a) the synthesis and characterization of 3,8-bis(4-mercaptophenyl)-1,10-phenanthroline and its ruthenium(II) complex, (b) single-crystal structures of four intermediates (**1**, **3**, **4**, and **7**) and one dithiol precursor (**8**) to obtain additional information on these molecules, and (c) temperature-dependent (7−300 K) $I-V$ measurements for the nanodevices wherein 3,8-bis(4-mercaptophenyl)-1,10-phenanthroline and its ruthenium(II) complex were self-assembled onto two facing gold electrodes with a 1 μm gap to form statically stable gold−sulfur−aryl−sulfur−gold junctions.

2. Results and Discussion

2.1. Synthesis. In this paper, a novel dithiol molecule 3,8-bis(4-mercaptophenyl)-1,10-phenanthroline and its ruthenium(II) complex were successfully obtained after a multistep synthesis as illustrated in Scheme 1. Compound **1** was prepared by the treatment of 3,8-dibromo-1,10-phenanthroline with the Grignard reagent prepared from 4-bromoanisole and magnesium. Compound **2** was obtained by heating a mixture of pyridinium chloride and **1** in a nitrogen atmosphere. The method used for producing **1** was different from that reported by Dietrich-Buchecker et al. where Suzuki cross-coupling condition was used.[12a] The method used for producing **2** was also different from the method used by Christophe et al.[12b] wherein freshly prepared sodium methoxide was utilized for the aromatic nucleophilic substitution and HBr/CH_3COOH was used as a hydrolysis reagent to only obtain the HBr salt of **1**. Compound **5** was obtained by the condensation of *N*,*N*′-dimethylthiocarbamoyl chloride and **2** in a catalytic amount of 4-*N*,*N*′-dimethylaminopyridine in dry pyridine. Compound **6** was synthesized by the Newman−Kwart rearrangement from **5** in an argon atmosphere in a glass tube oven at 300 °C for 6 h.[13]

In terms of organic synthesis, **1** is a very useful intermediate for preparing a number of compounds because two hydroxyl groups are chemically active and can be easily transformed to other functional groups for further study.[14] **1** can also be used to produce a single-electron transistor having uniform operating characteristics and various characteristics by introducing a ruthenium(II) ion into the system.[15]

All the Ru(II) complexes were produced by refluxing stoichiometric amounts of *cis*-bis(2,2′-bipyridine)dichlororuthenium(II) hydrate or *cis*-bis(1,10-phenanthroline)dichlo-

(1) (a) Park, J.; Pasupathy, A. N.; Goldsmith, J. I.; Chang, C.; Yaish, Y.; Petta, J. R.; Rinkoski, M.; Sethna, J. P.; Abruna, H. D.; McEuen, P. L.; Ralph, D. C. *Nature* **2002**, *417*, 722−725. (b) Liang, W. J.; Shores, M. P.; Bockrath, M.; Long, J. R.; Park, H. *Nature* **2002**, *417*, 725−729. (c) Carroll, R. L.; Corman, C. B. *Angew. Chem., Int. Ed.* **2002**, *41*, 4378−4440. (d) Kubatkin, S.; Danilov, A.; Hjort, M.; Cornil, J.; Bredas, J. L.; Stuhr-Hansen, N.; Hedegård, P.; Bjørnholm, T. *Nature* **2003**, *425*, 698−701. (e) Nitzan, A.; Ratner, M. A. *Science* **2003**, *300*, 1384−1389. (f) Xu, B.; Tao, N. J. *Science* **2003**, *301*, 1221−1223. (g) Schenning, A. P. H. J.; Meijer, E. W. *Chem. Communs.* **2005**, 3245−3258. (h) Murphy, A. R.; Fréchet, J. M. J. *Chem. Rev.* **2007**, **107**, 1066−1096.

(2) Reed, M. A.; Lee, T. *Molecular Nanoelectronics*; American Scientific Publishers: Los Angeles, CA, 2003.

(3) Skotheim, T. A. *Handbook of Conducting Polymers*; Dekker: New York, 1992.

(4) Robson, R.; Abrahams, B. F.; Batten, S. R.; Gable, R. W.; Hoskins, B. F.; Liu, J. *Supramolecular Architecture*; American Chemical Society: Washington, DC, 1992.

(5) Black, C. T.; Murray, C. B.; Sandstrom, R. L.; Sun, S. *Science* **2000**, *290*, 1131−1134.

(6) Baraton, M. I. *Synthesis, Functionalization and Surface Treatment of Nanoparticles*; American Scientific Publishers: Los Angeles, CA, 2003.

(7) See, for examples: (a) Terrill, R. H.; Postlethwaite, T. A.; Chen, C.; Poon, C. D.; Terzis, A.; Chen, A.; Hutchison, J. E.; Clark, M. R.; Wignall, G.; Londono, J. D.; Superfine, R;. Falvo, M.; Johnson, C. S., Jr.; Samulski, E. T.; Murray, R. W. *J. Am. Chem. Soc.* **1995**, *117*, 12537−12548. (b) Andres, R. P.; Bein, T.; Dorogi, M.; Feng, S.; Henderson, J. I.; Kubiak, C. P.; Mahoney, W.; Osifchin, R. G.; Reifenberger, R. *Science* **1996**, *272*, 1323−1325. (c) Kruger, D.; Fuchs, H.; Rousseau, R.; Marx, D.; Parrinello, M. *J. Chem. Phys.* **2001**, *115*, 4776−4786. (d) Mohamed, A. A.; Abdou, H. E.; Chen, J.; Bruce, A. E.; Bruce, M. R. M. *Comm. Inorg. Chem.* **2002**, *23*, 321−334.

(8) See, for examples: (a) Schlenoff, J. B.; Li, M.; Ly, H. *J. Am. Chem. Soc.* **1995**, *117*, 12528−12536. (b) Chi, Q. J.; Zhang, J. D.; Nielsen, J. U.; Friis, E. P.; Chorkendorff, I.; Canters, G. W.; Andersen, J. E. T.; Ulstrup, J. *J. Am. Chem. Soc.* **1995**, *122*, 4047−4055. (c) Li, X. M.; Huskens, J.; Reinhoudt, D. N. *J. Mater. Chem.* **2004**, *14*, 2954−2971. (d) Belser, T.; Stohr, M.; Pfaltz, A. *J. Am. Chem. Soc.* **2005**, *127*, 8720−8731.

(9) See, for examples: (a) Brust, M.; Bethell, D.; Kiely, C. J.; Schiffrin, D. J. *Langmuir* **1998**, *14*, 5425−5429. (b) Teranishi, T.; Haga, M.; Shiozawa, Y.; Miyake, M. *J. Am. Chem. Soc.* **2000**, *122*, 4237−4238. (c) Zamborini, F. P.; Hicks, J. F.; Murray, R. W. *J. Am. Chem. Soc.* **2000**, *122*, 4514−4515. (d) Kanehara, M.; Oumi, Y.; Sano, T.; Teranishi, T. *J. Am. Chem. Soc.* **2003**, *125*, 8708−8709. (e) Zhao, W.; Xu, J. J.; Shi, C. G.; Chen, H. Y. *Langmuir* **2005**, *21*, 9630−9634. (f) Minamoto, M.; Matsushita, M. M.; Sugawara, T. *Polyhedron* **2005**, *24*, 2263−2268.

(10) (a) Wada, Y.; Tsukada, M.; Fujihira, M.; Matsushige, K.; Ogawa, T.; Haga, M.; Tanaka, S. *Jpn. J. Appl. Phys.* **2000**, *39*, 3835−3849. (b) Ogawa, T.; Kobayashi, K.; Masuda, G.; Takase, T.; Maeda, S. *Thin Solid Films* **2001**, *393*, 374−378. (c) Ozawa, H.; Kawao, M.; Tanaka, H.; Ogawa, T. *Langmuir* **2007**, *23*, 6365−6371. (d) Ogawa, T.; Ozawa, H.; Kawao, M.; Tanaka, H. *J. Mater. Sci.: Mater. Electron* **2007**, *18*, 939−942.

(11) (a) Huang, W.; Masuda, G.; Maeda, S.; Tanaka, H.; Ogawa, T. *Chem. Eur. J.* **2006**, *12*, 607−619. (b) Ogawa, T.; Huang, W.; Tanaka, H. *Mol. Cryst. Liq. Cryst.* **2006**, *455*, 299−303.

(12) (a) Dietrich-Buchecker, C.; Jimenez, M. C.; Sauvage, J. P. *Tetrahedron Lett.* **1999**, *40*, 3395−3396. (b) Christophe, B.; Marguerite, P.; Bernard, M. *Synlett* **2001**, *10*, 1629−1631.

(13) (a) Newman, M. S.; Karnes, H. K. *J. Org. Chem.* **1966**, *31*, 3980−3984. (b) Kwart, H.; Evans, E. R. *J. Org. Chem.* **1966**, *31*, 410−413.

(14) Sammes, P. G.; Yahioglu, G. *Chem. Soc. Rev.* **1994**, 327−334.

Scheme 1. Schematic Illustration of the Preparation of the Compounds Used in the Present Study

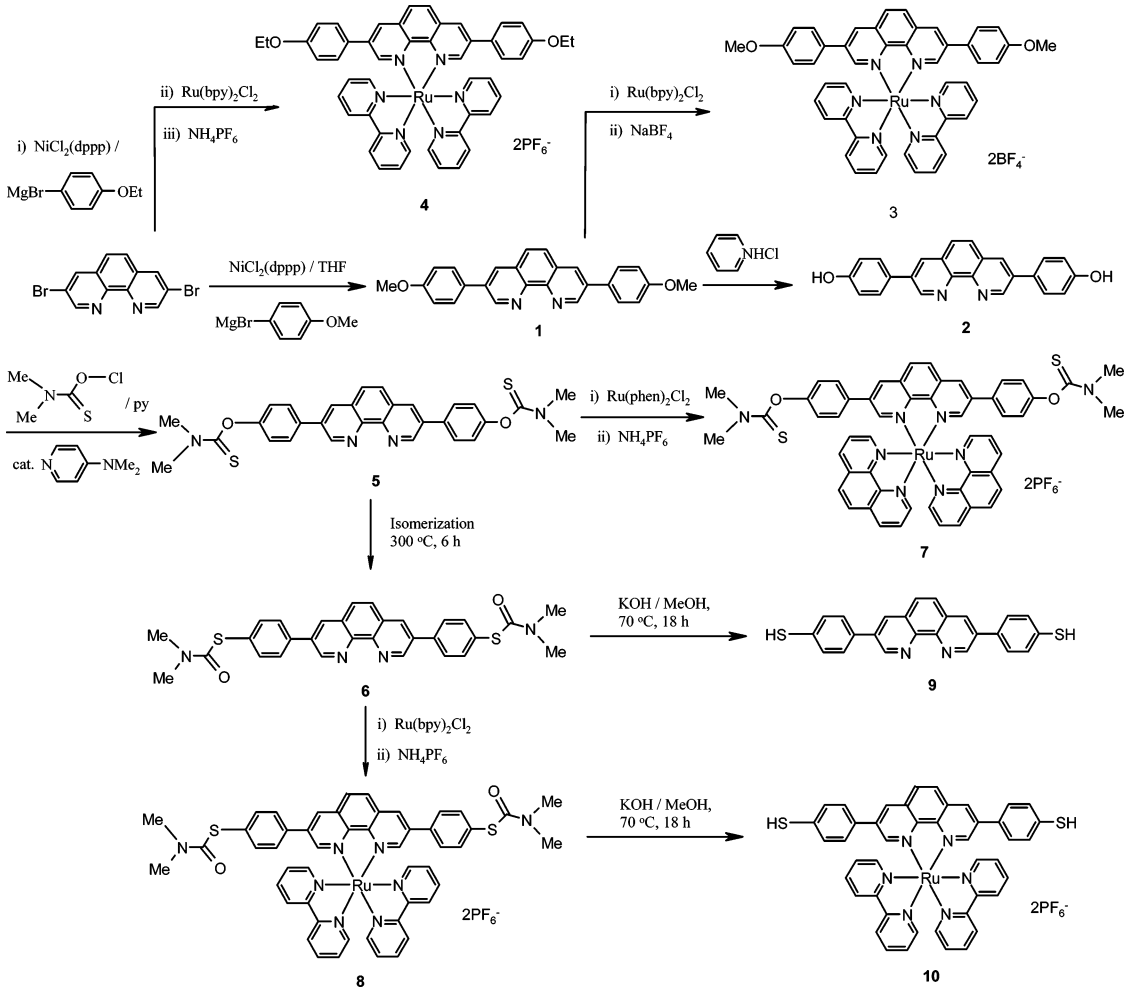

roruthenium(II) and their respective ligands in methanol and then treating in situ anion exchange by adding excess NH_4PF_6 or $NaBF_4$ in order to precipitate the complexes from their mother solutions. Successful preparation of dithiols **9** and **10** by hydrolysis in the presence of KOH was checked using thin layer chromatography (TLC) and by the presence of a new single peak at 3.69 ppm for **9** and 3.56 ppm for **10** in their respective ^{1}H NMR spectra. However, due to the influence of the strong coordination ability of the mercapto groups and the possible oxidative oligomerization of dithiols in the ligand, direct synthesis from **9** to **10** was unsuccessful. The yield is very low, and it is very difficult to purify the desired product.

All synthetic steps gave moderate to high yields, making the strategy convenient for the preparation of these functionalized 3,8-bisphenyl-1,10-phenanthroline derivatives. Infrared, UV−vis, and NMR spectroscopies, mass spectrometry, and elemental analyses of the compounds were performed and consistent with the structures shown in Scheme 1. In addition, compounds **1**, **3**, **4**, **7**, and **8** were further characterized by X-ray single-crystal diffraction experiments. The results of the last four six-coordinate Ru(II) complexes revealed that they all crystallize in the centrosymmetric space group, indicative of the presence of an equal amount of Δ and Λ enantiomers in their solid state.[16,17]

The self-assembled ditiol/Au-NPs nanocomposite films could be achieved simply by mixing freshly prepared dithiol and active monothiol-ligated Au-NPs[18] in the presence of Au gap electrodes at room temperature. The dithiol-bridged Au-NPs were likely formed within the solution and adhered to the surfaces of two facing Au electrodes as well as an area around them after an in situ thiol-to-thiol ligand exchange reaction.

2.2. Structural Description of 1, 3, and 4. The molecular structures of **1**, **3**, and **4** dications with atom-numbering scheme are shown in Figures 1 and 2, respectively. Compound **1** crystallizes in the orthorhombic system of the noncentrosymmetric space group $Pna2_1$. The central phenanthroline ring and two phenyl rings are not coplanar with bite angles of 29.8° and 35.7°, respectively, due to the free rotation of the C−C σ bond. Two terminal methyl groups adopt a cis configuration with respect to the whole molecular plane, and the separation between the O1 and O2 atoms is

(15) Ogawa, T.; Endo, H. Japan Patent JP2004059552, 2004.

(16) von Zelewsky, A.; Mamula, O. *J. Chem. Soc., Dalton Trans.* **2000**, 219−231.
(17) Huang, W.; Ogawa, T. *Polyhedron* **2006**, *25*, 1379−1385.
(18) Araki, K.; Mizuguchi, E.; Tanaka, H.; Ogawa, T. *J. Nanosci. Nanotechnol.* **2006**, *6*, 708−712.

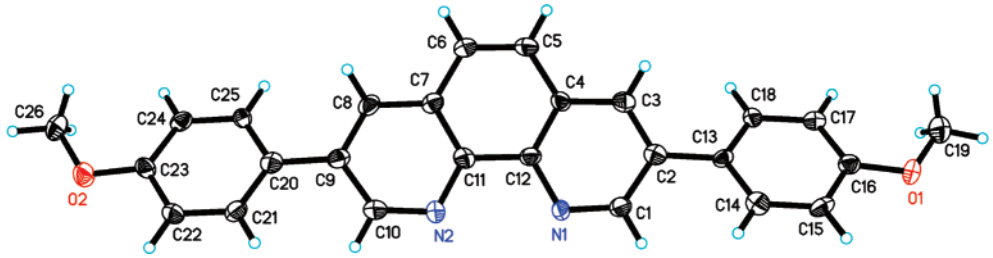

Figure 1. ORTEP diagram (30% thermal probability) of the molecular structure of **1** with atom-numbering scheme.

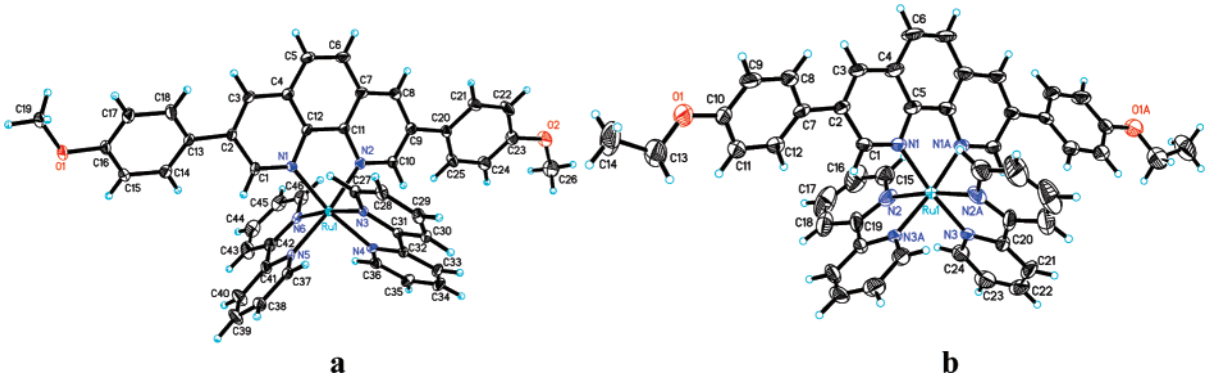

Figure 2. ORTEP diagrams (30% thermal probability) of the molecular structures of (a) **3** and (b) **4** with atom-numbering scheme. Anions and solvent molecules are omitted for clarity.

1.827 nm. In the crystal packing of **1**, about one-half of the phenyl ring's shift is observed between vicinal molecules, forming an offset layer-packing mode. The centroid−centroid distances between one middle ring of phenanthroline and two adjacent rings in a head-to-tail mode are 3.867 and 3.996 Å, exhibiting typical $\pi-\pi$ stacking interactions (see Figure 8 in Supporting Information). Thus, an ordered 1D layer packing structure is constructed wherein all the phenanthroline planes are perpendicular to the crystallographic *c* axis.

3 and **4** crystallize in different space groups *P*-1 (**3**) and *C*2/c (**4**) with different crystallographic symmetry. Two lattice water molecules are present in each asymmetric unit cell of **3**, and three acetone molecules are found in each asymmetric unit cell of **4**. The ruthenium(II) centers are coordinated by six nitrogen atoms from one 3,8-disubstituted phenanthroline and two bidentate 2,2′-bipyridine ligands, adopting distorted octahedrons. The dihedral angles between the central phenanthroline ring and two phenyl rings are 29.8° and 33.2° in **3** and 32.1° in **4**, respectively. The distances between two terminal oxygen atoms are 1.81 nm in **3** and 1.82 nm in **4**.

It is interesting to mention that $\pi-\pi$ stacking interactions are present in different strengths in the crystal-packing structures of **3** and **4**. Neighboring phenyl rings of the molecules are parallel with centroid−centroid separations of 3.74 Å in **3** and 3.95 Å in **4** (see Figure 9a and 9b in Supporting Information). The different packing modes of **3** and **4** contribute significantly to the difference in the UV−vis spectra in the solid state, although they have almost the same absorptions in methanol, which will be discussed below. In addition, O−H···F and O−H···O hydrogen bonds are observed between the lattice water molecules and the BF_4^- anions in **3**, and weak C−H···F and C−H···O hydrogen bonds are found in **3** and **4** which can further stabilize the structures.

2.3. Single-Crystal Structures of 7 and 8. Ru(II) complexes **7** and **8** pack into the same centrosymmetric space group *P*-1. There are two water molecules in the asymmetric unit of **7**, while three chloroform molecules are present in the asymmetric unit of **8**. As illustrated in Figure 3, both ruthenium(II) centers are coordinated by six nitrogen atoms from one 3,8-disubstituted phenanthroline and two bidentate 1,10-phenanthroline (**7**) or 2,2′-bipyridine (**8**) ligands, showing distorted octahedral coordination spheres. The dihedral angles between the central phenanthroline ring and two phenyl rings are 43.1° and 41.2° in **7** and 33.3° and 40.6° in **8**, respectively. The dihedral angles among three phenanthroline rings around the Ru(II) center in **7** are 97.1°, 85.0°, and 80.6°, while those between the phenanthroline ring and two 2,2′-bipyridine rings in **8** are almost perpendicular (91.7° and 93.4°), and the dihedral angle between two 2,2′-bipyridine rings is 82.4°. The separation between the terminal oxygen atoms in **7** is 1.77 nm (O1−O2), and the centroid−centroid separation between two adjacent phenanthroline rings is 3.524 Å (see Figure 10 in Supporting Information) showing typical $\pi-\pi$ stacking interactions. In contrast, the distance between the terminal sulfur atoms in **8** is 1.89 nm (S1−S2). Similarly, weak C−H···F, C−H···O, C−H···N, and C−H···S hydrogen bonds are observed in the crystal-packing structures of **7** and **8** to minimize the total energies of the molecules and help form the resulting hydrogen-bond-sustained networks.

The study of these single-crystal structures, especially for the ruthenium complexes, is interesting in terms of the coordination chemistry,[19] photochemistry,[20] and stereochemistry.[14,15] Until now, there have been only two related

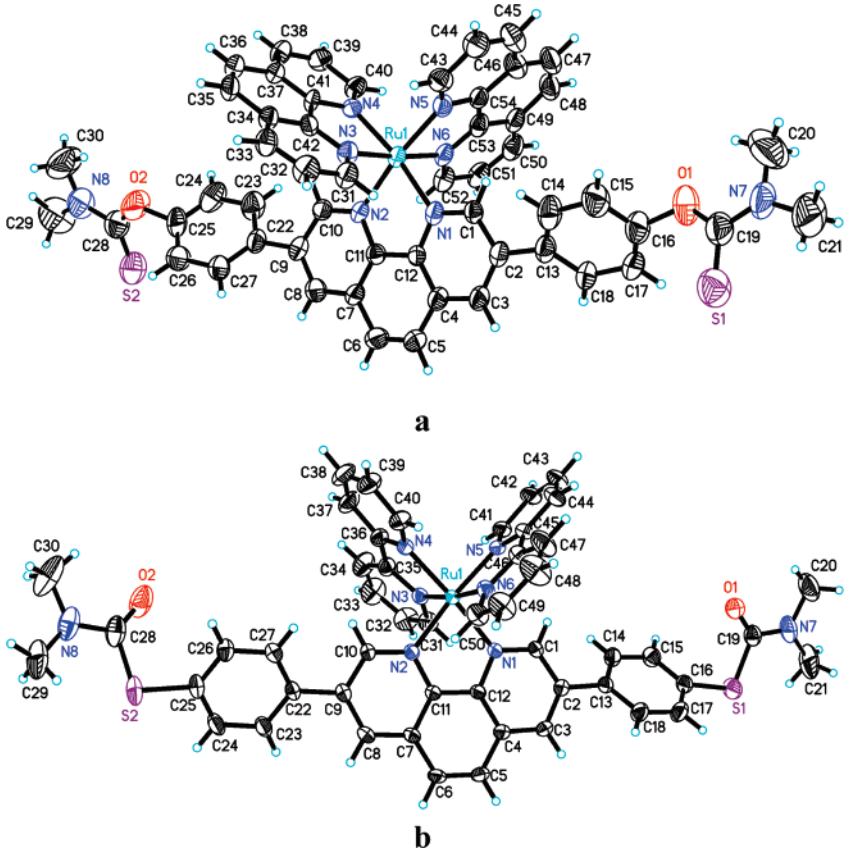

Figure 3. ORTEP views (30% thermal probability) of the molecular structures of (a) **7** and (b) **8** with atom-numbering scheme. Anions and solvent molecules have been left out for simplicity.

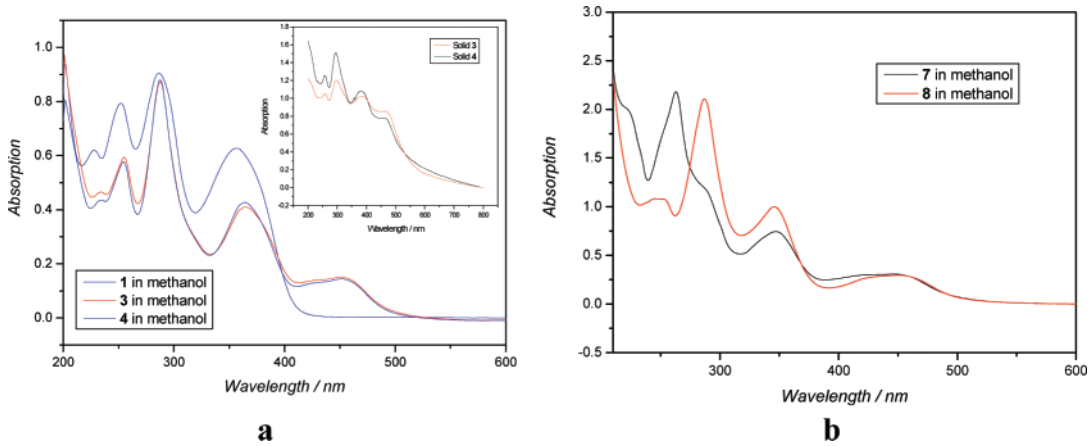

Figure 4. (a) Electronic absorption spectra of **1** (black line), **3** (red line), and **4** (blue line) in methanol. The inset shows the electronic absorption spectra of **3** (red line) and **4** (black line) in the solid state. (b) Electronic absorption spectra of **7** and **8** in methanol.

structural reports on 3,8-bisphenyl-1,10-phenanthroline derivatives, by checking the Cambridge Structural Database (Version 5.28).[21] Both of the structures are involved in copper(I)-directed self-assemblies, i.e., a doubly threaded dinuclear Cu(I) complex having a chelating ring substituted 3,8-bis(4-hydroxyphenyl)-1,10-phenanthroline ligand[22] and a tetranuclear Cu(I) biphenanthroline gridwork.[23]

2.4. Electronic Spectra. UV−vis spectra of **1**, **3**, and **4** in methanol and in the solid state were measured. As shown in Figure 4a, UV−vis spectra of **3** and **4** are very similar in

(19) Balzani, V.; Juris, A.; Venturi, M.; Campagna, S.; Serroni, S. *Chem. Rev.* **1996**, *96*, 759−834.
(20) (a) Kalyanasundaram, K. *Coord. Chem. Rev.* **1982**, *46*, 159−244. (b) Juris, A.; Barigelletti, S.; Campagna, S.; Balzani, V.; Belser, P.; Zelewsky, von A. *Coord. Chem. Rev.* **1988**, *84*, 85−277. (c) Xu, Y.; Eilers, G.; Borgström, M.; Pan, J.; Abrahamsson, M.; Magnuson, A.; Lomoth, R.; Bergquist, J.; Polívka, T.; Sun, L.; Sundström, V.; Styring, S.; Hammarström, L.; Åkermark, B. *Chem. Eur. J.* **2005**, *11*, 7305−7314.
(21) Allen, F. H. *Acta Crystallogr., Sect. B* **2002**, *58*, 380−388.
(22) (a) Jimenez, M. C.; Dietrich-Buchecker, C.; Sauvage, J. P.; Cian, A. De *Angew. Chem., Int. Ed.* **2000**, *39*, 1295−1298. (b) Jimenez, M. C.; Dietrich-Buchecker, C.; Sauvage, J. P. *Chem. Eur. J.* **2002**, *8*, 1456−1466.
(23) Toyota, S.; Woods, C. R.; Benaglia, M.; Haldimann, R.; Wärnmark, K.; Hardcastle, K.; Siegel, J. S. *Angew. Chem., Int. Ed.* **2001**, *40*, 752−754.

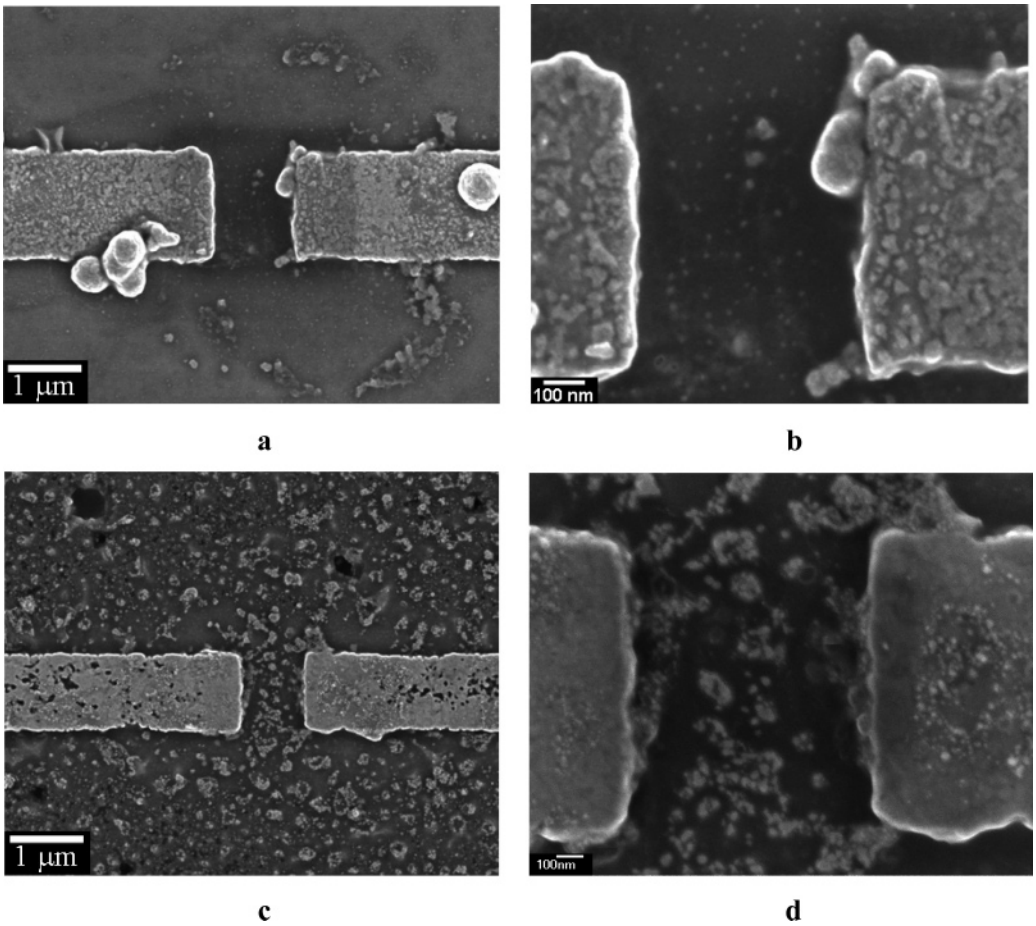

Figure 5. SEM images of the self-assembled films composed of **9**/Au-NPs (a and b) and **10**/Au-NPs (c and d) on the surface of 1 μm gap gold electrodes with different magnifications.

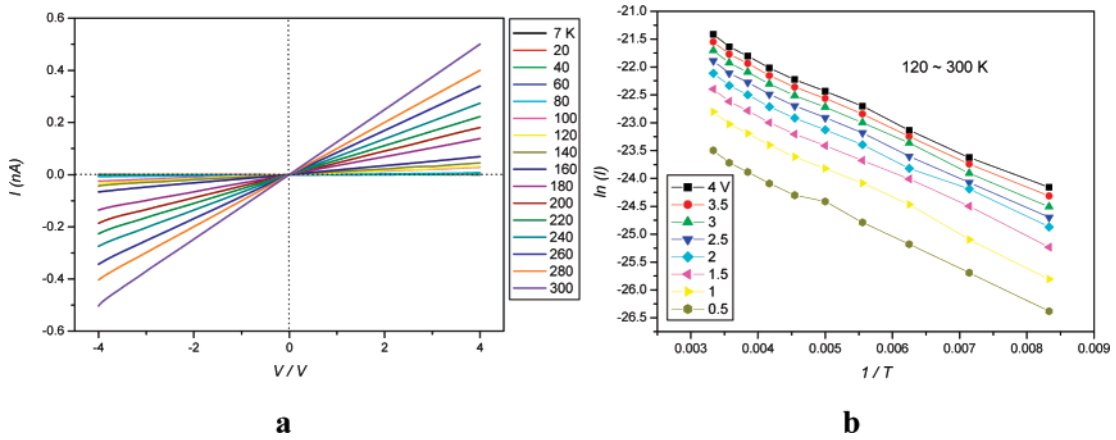

Figure 6. $I-V$ characteristics of a molecular junction consisting of **9**/Au-NPs covering two facing Au electrodes with a 1 μm gap. (a) Full range of the $I-V$ curves from 7 to 300 K with intervals of 20 K in the voltage range from −4 to 4 V. (b) Classical Arrhenius plots at 0.5−4 V with a step of 0.5 V in the temperature range of 120−300 K.

methanol because they have almost the same π-conjugated systems with respect to their molecules. In comparison with **1**, new broad but weak peaks at 451 nm were observed for Ru(II) complexes **3** and **4**, corresponding to the metal−ligand charge transfer (MLCT) absorptions. In comparison with the same absorptions in methanol, lower energy absorptions and red shifts were observed for the crystalline solids (inset in Figure 4a), which is a reflection of their solid structures. As mentioned above, complex **3** has much stronger $\pi-\pi$ stacking interactions between molecules in its packing structure than **4**, which offers a greater possibility for intermolecular charge transfer or delocalization of the excited energy. Consequently, MLCT red shifts of 11 and 7 nm were recorded from the methanol solutions to the solids of **3** to **4**, and a 4 nm red shift (from 462 to 458 nm) was observed on going from **3** to **4**.

UV−vis spectra of **7** and **8** in methanol are shown in Figure 4b. Low-energy MLCT bands were recorded at 446

Table 1. Crystal and Refinement Data for Five Compounds

	1	3	4	7	8
empirical formula	$C_{26}H_{20}N_2O_2$	$[Ru(C_{46}H_{36}N_6O_2)](BF_4)_2 \cdot (H_2O)_2$	$[Ru(C_{48}H_{40}N_6O_2)](PF_6)_2 \cdot (CH_3COCH_3)_3$	$[Ru(C_{54}H_{42}N_8O_2S_2)](PF_6)_2 \cdot (H_2O)_2$	$[Ru(C_{50}H_{42}N_8O_2S_2)](PF_6)_2 \cdot (CHCl_3)_3$
fw	392.44	1015.53	1298.10	1326.12	1600.15
T/K	291(2)	153(2)	100(2)	291(2)	291(2)
wavelength/Å	0.71073	0.71073	0.71073	0.71073	0.71073
cryst size (mm)	0.30 × 0.10 × 0.10	0.30 × 0.10 × 0.10	0.10 × 0.10 × 0.10	0.35 × 0.20 × 0.10	0.40 × 0.10 × 0.10
cryst syst	orthorhombic	triclinic	monoclinic	triclinic	triclinic
space group	$Pna2_1$	$P\bar{1}$	$C2/c$	$P\bar{1}$	$P\bar{1}$
a, Å	11.727(2)	12.017(2)	17.066(3)	12.628(4)	12.965(3)
b, Å	22.889(5)	13.253(3)	15.451(3)	14.164(3)	15.152(3)
c, Å	7.1966(14)	13.795(3)	22.363(5)	17.623(3)	18.160(4)
α, deg	90.00	81.88(3)	90.00	68.05(2)	75.62(3)
β, deg	90.00	84.83(3)	96.73(3)	76.46(2)	78.02(3)
γ, deg	90.00	82.76(3)	90.00	81.09(2)	72.31(3)
V, Å^3	1931.8(7)	2151.8(8)	5856(2)	2834.5(13)	3258.4(13)
Z/D_{calcd} (g/cm^3)	4/1.349	2/1.567	4/1.472	2/1.554	2/1.631
F(000)	824	1032	2720	1344	1604
μ, mm^{-1}	0.086	0.452	0.413	0.499	0.804
abs corr	multiscan	multiscan	multiscan	multiscan	multiscan
min/max transmission	0.976/0.991	0.876/0.956	0.960/0.961	0.845/0.952	0.739/0.924
refinement method	full-matrix least-squares on F^2	full-matrix least-squares on F^2	full-matrix least-squares on F^2	full-matrix least-squares on F^2	full-matrix least-squares on F^2
h_{min}/h_{max}	−13/12	−14/12	−20/20	−14/15	−15/15
k_{min}/k_{max}	−26/27	−14/15	−17/18	−14/16	−16/18
l_{min}/l_{max}	−8/7	−15/16	−26/25	−19/20	−20/21
parameters	273	600	424	781	862
final R indices $[I > 2\sigma(I)]$[a]	$R1 = 0.0813$, $wR2 = 0.1448$	$R1 = 0.0614$, $wR2 = 0.1343$	$R1 = 0.0981$, $wR2 = 0.2057$	$R1 = 0.0988$, $wR2 = 0.2109$	$R1 = 0.0698$, $wR2 = 0.1602$
R indices (all data)	$R1 = 0.0883$, $wR2 = 0.1480$	$R1 = 0.0672$, $wR2 = 0.1376$	$R1 = 0.1259$, $wR2 = 0.2165$	$R1 = 0.1289$, $wR2 = 0.2287$	$R1 = 0.0776$, $wR2 = 0.1648$
goodness-of-fit on F^2	1.059	1.022	1.267	1.012	0.939
max/min, $\Delta\rho$ (e·Å^{-3})	0.185, −0.178	1.686, −1.222	0.848, −1.007	0.494, −0.559	0.869, −0.970

[a] $R1 = \Sigma||F_o| - |F_c||/\Sigma|F_o|$, $wR2 = [\Sigma[w(F_o^2 - F_c^2)^2]/\Sigma w(F_o^2)^2]^{1/2}$.

nm for **7** and 451 nm for **8**, respectively, which are consistent with their molecular structures since the phenyl−S bond has a better ability to promote charge separation compared to the phenyl−O bond. In contrast, this MLCT peak cannot be observed in ligand **6**. At the high-energy band, the $\pi \rightarrow \pi^*$ charge-transfer absorption at 287 nm for **8** is strengthened when 2,2′-bipyridine is replaced with 1,10-phenanthroline.[15,24]

2.5. Thermal Analysis of 7 and 8. TGA-DTA analyses of Ru(II) complexes **7** and **8** showed that **7** is a little more thermally stable than **8**, which can be explained by the stronger complexation of 1,10-phenanthroline with the ruthenium(II) center, i.e., different Ru−N bond lengths for **7** and **8**, as shown in Table 2. Specifically, they remained unchanged (no weight loss) until 350 °C for **7** and 335 °C for **8**, respectively, and then they decomposed where two DTA peaks were recorded during this process, i.e., peaks at 374 and 436 °C for **7** and those at 359 and 420 °C for **8**, respectively.

2.6. Electrochemistry of 8 and 10. The electrochemical behavior of 3,8-bisphenyl-1,10-phenanthroline-derivatived ruthenium(II) complexes **8** and **10** is analogous to those of 3,8-bisthiophenyl-1,10-phenanthroline and 3,8-bisterthiophenyl-1,10-phenanthroline $[Ru(bpy)_2]^{2+}$ complexes (Table 3), which have been elaborately described in one of our previous reports.[25] Complex **8** exhibited five reversible monoelectronic processes at 0.97, −1.17, −1.52, −1.77, and −1.99 V versus saturated calomel electrode (SCE) in the scan range from 1.45 to −2.70 V in acetonitrile solution, while those for complex **10** were found at 1.00, −1.18, −1.56, −1.80, and −2.07 V versus SCE, respectively. The reversible redox couples at 0.97 V in **8** and 1.00 V in **10** correspond, without doubt, to the Ru^{II}/Ru^{III} process, which are lower than 1.26 V in $[Ru(bpy)_2(phen)]^{2+}$ and $[Ru(bpy)_3]^{2+}$ complexes[20,26] due to the presence of more delocalized π systems. The reduction process at −1.17 V in **8** (−1.18 V in **10**) is attributed to the monoelectronic reduction of the phenanthroline ligand, and the following two processes at −1.52 and −1.77 V in **8** (−1.56 and −1.80 V in **10**) are then ascribed to the successive monoelectronic reductions of each bpy ligand in **8** and **10**, respectively. Similarly, the last process is tentatively attributed to the second monoelectronic reduction of the substituted phenanthroline ligand. All processes were also diffusion controlled, as attested by the linear relationship between the current and the square root of the scan rate.

2.7. SEM Images of Self-Assembled Nanocomposite Films for 9- and 10-Bridged Au-NPs. SEM images of representative junctions, where 0.1 mmol/L solutions are used for preparing the self-assembled thin films composed of **9** and **10**-bridged Au-NPs on the surface of 1 × 1 μm^2 gap Au electrodes, are shown in Figure 5 at different magnifica-

(24) Ye, B. H.; Chen, X. M.; Zeng, T. X.; Ji, L. N. *Inorg. Chim. Acta* **1995**, *240*, 5−11.

(25) Araki, K.; Endo, H.; Masuda, G.; Ogawa, T. *Chem. Eur. J.* **2004**, *10*, 3331−3340.

(26) (a) Pappenfus, T. M.; Mann, K. R. *Inorg. Chem.* **2001**, *40*, 6301−6307. (b) Walters, K. A.; Trouillet, L.; Guillerez, S.; Schanze, F. S. *Inorg. Chem.* **2000**, *39*, 5496−5509. (c) Belser, P.; Zelewsky, A. V. *Helv. Chim. Acta* **1980**, *63*, 1675−1702.

Table 2. Selected Bond Distances (Å) and Angles (deg) in **1**, **3**, **4**, **7**, and **8**

bond distances		bond angles	
	1		
O1−C16	1.374(6)	C16−O1−C19	115.6(5)
O1−C19	1.450(10)	C23−O2−C26	116.1(5
O2−C23	1.373(6)		
O2−C26	1.431(9)		
N1−C1	1.314(6)		
N1−C12	1.368(6)		
N2−C10	1.325(6)		
N2−C11	1.351(7)		
	3		
Ru1−N1	2.051(4)	N1−Ru1−N2	80.2(2)
Ru1−N2	2.081(4)	N1−Ru1−N3	95.5(2)
Ru1−N3	2.052(4)	N1−Ru1−N4	170.2(2)
Ru1−N4	2.059(4)	N1−Ru1−N5	93.9(2)
Ru1−N5	2.057(4)	N1−Ru1−N6	89.7(2)
Ru1−N6	2.052(4)	C16−O1−C19	116.0(4)
O1−C16	1.375(5)	C23−O2−C26	118.0(4)
O1−C19	1.411(6)		
O2−C23	1.372(7)		
O2−C26	1.433(8)		
	4		
Ru1−N1	2.055(7)	N1−Ru1−N2	86.2(3)
Ru1−N2	2.028(7)	N1−Ru1−N3	173.2(3)
Ru1−N3	2.039(7)	N2−Ru1−N3	96.5(3)
		C10−O1−C13	120.4(10)
	7		
Ru1−N1	2.037(5)	N1−Ru1−N2	80.9(2)
Ru1−N2	2.010(6)	N1−Ru1−N3	95.3(2)
Ru1−N3	2.057(7)	N1−Ru1−N4	171.5(2)
Ru1−N4	2.031(5)	N1−Ru1−N5	94.2(2)
Ru1−N5	2.016(6)	N1−Ru1−N6	88.2(2)
Ru1−N6	2.064(7)	C16−O1−C19	122.7(11)
S1−C19	1.571(2)	C25−O2−C28	118.9(10)
S2−C28	1.565(2)	O1−C19−N7	111.1(15)
O1−C16	1.442(2)	S1−C19−O1	125.3(13)
O1−C19	1.290(2)	S1−C19−N7	123.7(12)
O2−C25	1.427(1)	S2−C28−O2	125.7(9)
O2−C28	1.337(2)	S2−C28−N8	126.6(11)
		O2−C28−N8	107.7(13)
	8		
Ru1−N1	2.074(4)	N1−Ru1−N2	79.7(1)
Ru1−N2	2.081(3)	N1−Ru1−N3	97.9(2)
Ru1−N3	2.059(4)	N1−Ru1−N4	175.6(2)
Ru1−N4	2.062(4)	N1−Ru1−N5	95.7(1)
Ru1−N5	2.056(3)	N1−Ru1−N6	88.2(2)
Ru1−N6	2.067(4)	C16−S1−C19	100.4(3)
S1−C16	1.788(6)	C25−S2−C28	102.0(3)
S1−C19	1.786(6)	S1−C19−O1	121.2(4)
S2−C25	1.767(6)	O1−C19−N7	124.2(6)
S2−C28	1.767(6)	S1−C19−N7	114.6(5)
O1−C19	1.199(7)	S2−C28−O2	124.0(6)
O2−C28	1.221(11)	O2−C28−N8	124.0(8)
		S2−C28−N8	112.0(6)

Table 3. Redox Potentials (V versus SCE) of the Ruthenium Complexes **8** and **10** in This Work and a Previously Reported Similar Ruthenium Complex[25] in Their Acetonitrile Solutions

complex	E_{ox} (Ru^{II}/Ru^{III})	L/L^-	$bpy_1^{0/-}$	$bpy_2^{0/-}$	L^-/L^{2-}
8	0.97	−1.17	−1.52	−1.77	−1.99
10	1.00	−1.18	−1.56	−1.80	−2.07
$[Ru(bpy)_2$(3,8-di(thiophen-2,2-yl)-1,10-phen)$](PF_6)_2$	1.32	−1.17	−1.44	−1.67	−1.97

tions. Different from the morphologies of our previously reported oligothiophene dithiol-bridged Au-NPs nanocomposite films,[11] the dithiol-capped Au-NPs in the present two cases were found to aggregate to a different extent, especially on the topmost layer. Homogeneous granular films cannot be achieved for both **9**/Au-NPs and **10**/Au-NPs systems; however, Ru(II) complex **10**-bridged Au-NPs are easier to aggregate into bigger particles than ligand **9**-bridged Au-NPs, which can be deduced by the size of big particles in SEM images. In addition, the self-assembled thin films favor forming on the surfaces of Au electrodes, where many more molecules were found (see also Figure 11a and 11b in the Supporting Information) due to the presence of Au−S-bonded contacts.

Although it is very difficult to give the specific growth mechanism of the self-assembled film, we think these phenomena are likely originated from the conformation and delocalized π-conjugated system of molecules. Here dithiol ligand **9** can only be regarded as a quasi-linear molecule, while Ru(II) complex **10** is in a quasi-spherical conformation. On the basis of previous results,[7a] it is known that long and linear terminal dithiols tend to form well-oriented films since long chain structures are easier to form the optimal conformation so as to reduce the steric hindrance among adjacent molecules in the process of self-assembly. Thus, both **9**/Au-NPs and **10**/Au-NPs nanocomposite systems tend to aggregate due to their short delocalized π-conjugated structures, and the latter is more likely to aggregate into bigger spheres compared with the former one due to its molecular conformation. Another reason for aggregation may come from the oxidative oligomerization of dithiols, which is still one of the serious drawbacks of thiol chemistry. Furthermore, it is suggested that the noncharged status of dithiol **9** and bivalent Ru(II) cation of **10** may also be responsible for the aggregation of dithiol-capped Au-NPs to a different extent because the Au-NPs are negatively charged (prepared from $HAuCl_4$ by $NaBH_4$ reduction in the presence of phase transfer catalyst) and very highly reactive. Anyway, these SEM images clearly indicate formation of self-assembled nanocomposite films between the micrometer gap Au electrodes, which make it possible to determine the temperature-dependent $I-V$ curves between them.

2.8. Current−Voltage Characteristics and Comparisons of Self-Assembled Films for 9- and 10-Bridged Au-NPs in the Temperature Range 7−300 K. In addition to comparing the SEM images of the gold electrodes before and after self-assembly (see Figure 11c in Supporting Information for one SEM image of the bare Au electrodes), a more reliable way is to verify the change of conductivity between the microgap Au electrodes before and after nanofabrication. In our experiment, no current can be observed between the bare Au electrode pairs, but an obvious change of conductivity can be recorded once the semiconductor self-assembled films are formed between them. The molecular junctions prepared in the present study are stable in air when different concentrations of Au-NPs and dithiols (0.05, 0.1, and 0.5 mmol/L) are used, and they can be kept unchanged over a large range of bias voltage under repeated cycling. Reproducible temperature-dependent $I-V$ curves were recorded using the cyclic scanning mode from 7 to 300 K with intervals of 20 K in the voltage range from −4 to 4 V with a scanning step of 0.05 V. In order to compare the

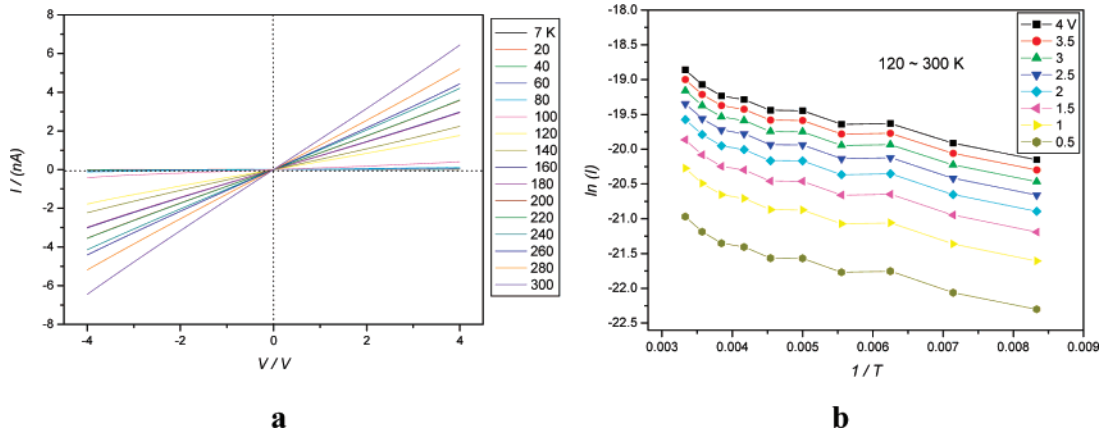

Figure 7. $I-V$ characteristics of a molecular junction consisting of **10**/Au-NPs covering two facing Au electrodes with a 1 μm gap. (a) Full range of the $I-V$ curves from 7 to 300 K with intervals of 20 K in the voltage range from −4 to 4 V. (b) Classical Arrhenius plots at 0.5−4 V with a step of 0.5 V in the temperature range of 120−300 K.

$I-V$ characteristics of **9**/Au-NPs junction and **10**/Au-NPs junction, the same experimental condition is used to fabricate the self-assembled nanocomposite films.

The full range of temperature-dependent (7−300 K) $I-V$ curves of one representative junction are shown in Figure 6a for **9**-bridged Au-NPs where 0.1 mmol/L reaction solutions were used for preparation. For this nanodevice small amounts of current on the order of pA could only be recorded at low temperature (<100 K), which means very little contribution of the temperature-independent tunneling current for the whole conductivity. Nevertheless, stable $I-V$ curves were obtained when the temperature exceeded 100 K, and the $I-V$ curves were almost linear in the high-temperature region, showing the typical ohmic conductance. The currents increased with increasing temperature and reached a maximum of 0.5 nA at 300 K and 4 V with a resistance on the order of 8.04×10^9 ohm. Since our previous studies indicated that thermal excitation current, wherein thermally excited extra charge carriers take part in the hopping process, contributes significantly to the conduction mechanism of this type of junctions, the Arrhenius equation can be used to calculate their average activation energy in the high-temperature region.[11] As can be seen in Figure 6b, when classical Arrhenius plots were done, nearly linear curves were obtained and the linear fits for eight curves at different bias voltages yielded an average activation energy of $\Delta E = 47$ meV in the 120−300 K and 0.5−4 V regions for this nanodevice. The resulting intercept (b) for two films, corresponding to pre-exponential terms of the Arrhenius equation, is obviously different. For example, at 4 V these values are −19.71 and −18.29 for **9**/Au-NPs and **10**/Au-NPs nanocomposite films, respectively, which may reflect the nature of nanocomposite films before and after metal-ion complexation. In addition, the differential intercept (Δb) of the fitted lines agrees well with $In(V_n + 0.5) - \mathrm{In}(V_n)$ (V_n = 0.5, 1, 1.5, 2, 2.5, 3, and 3.5 V), indicative of the voltage-dependent mechanism of the hopping conductance.[2] This ΔE value is close to that of a terthiophene-involved self-assembled thin film (50 meV), which was prepared under similar experimental conditions, even if the conductivity of this junction is only 1% of the terthiophene case at 300 K and 4 V.[11a]

In comparison with the dithiol ligand **9**/Au-NPs junction, the device $I-V$ characteristics of Ru(II) complex **10**/Au-NPs junction are similar after metal-ion complexation. However, the molecular junction conductance is increased at every temperature under the same experimental condition, as can be seen in Figure 7a. Similarly, by performing classical Arrhenius plots at the same temperature and voltage region (120−300 K and 0.5−4 V) (Figure 7b) and subsequent linear fits, a lower average activation energy of $\Delta E = 24$ meV can be obtained for nanocomposite film **10**. Molecular-based junctions **9**/Au-NPs and **10**/Au-NPs prepared from 0.05 and 0.5 mmol/L solutions give different amounts of current (higher conductance can be observed for thicker films) but analogous activation energy.

The difference in resistivity of these nanocomposite films is somewhat related to the band gaps of molecules which determine most of the electronic properties of the solid.[28] Density function theory (DFT) computations are carried out with the Gaussian 03, Revision C.02 program[27] using the MPW1PW91 method and LanL2DZ basis set. The fixed atom coordinates of **9** and **10**, originating from the structural parameters of **8** determined by the X-ray diffraction method, are used for the highest occupied molecular orbital (HOMO)

(27) Frisch, M. J.; Trucks, G. W.; Schlegel, H. B.; Scuseria, G. E.; Robb, M. A.; Cheeseman, J. R.; Montgomery, J. A.; Vreven, T., Jr.; Kudin, K. N.; Burant, J. C.; Millam, J. M.; Iyengar, S. S.; Tomasi, J.; Barone, V.; Mennucci, B.; Cossi, M.; Scalmani, G.; Rega, N.; Petersson, G. A.; Nakatsuji, H.; Hada, M.; Ehara, M.; Toyota, K.; Fukuda, R.; Hasegawa, J.; Ishida, M.; Nakajima, T.; Honda, Y.; Kitao, O.; Nakai, H.; Klene, M.; Li, X.; Knox, J. E.; Hratchian, H. P.; Cross, J. B.; Adamo, C.; Jaramillo, J.; Gomperts, R.; Stratmann, R. E.; Yazyev, O.; Austin, A. J.; Cammi, R.; Pomelli, C.; Ochterski, J. W.; Ayala, P. Y.; Morokuma, K.; Voth, G. A.; Salvador, P.; Dannenberg, J. J.; Zakrzewski, V. G.; Dapprich, S.; Daniels, A. D.; Strain, M. C.; Farkas, O.; Malick, D. K.; Rabuck, D.; Raghavachari, K.; Foresman, J. B.; Ortiz, J. V.; Cui, Q.; Baboul, A. G.; Clifford, S.; Cioslowski, J.; Stefanov, B. B.; Liu, G.; Liashenko, A.; Piskorz, P.; Komaromi, I.; Martin, R. L.; Fox, D. J.; Keith, T.; Al-Laham, M. A.; Peng, C. Y.; Nanayakkara, A.; Challacombe, M.; Gill, P. M. W.; Johnson, B.; Chen, W.; Wong, M. W.; Gonzalez, C.; Pople, J. A. *Gaussian 03*, Revision C.02; Gaussian, Inc.: Pittsburgh, PA, 2004.
(28) (a) Hill, I. G.; Kahn, A.; Soos, Z. G.; Pascal, R. A., Jr. *Chem. Phys. Lett.* **2000**, *327*, 181−188. (b) Zahn, D. R. T.; Gavrila, G. N.; Salvan, G. *Chem. Rev.* **2007**, *107*, 1161−1232 and references therein.

and lowest unoccupied molecular orbital (LUMO) gap calculation. The resultant band gaps (HOMO−LUMO gaps) for ligand **9** and Ru(II) complex **10** are 4.149 and 2.614 eV (2.476 eV for the dication of **10**), respectively. Thus, one can see that introduction of Ru(II) ion into the system plays a significant role in decreasing the band gaps of molecules, where the transportation of electrons from the HOMO to the LUMO can be greatly facilitated when excited. As a result, the observed conductivity of nanodevice **10**/Au-NPs is increased after the Ru(II)-ion complexation.

The barriers to injection for molecule-dependent nanocomposite films are mainly attributed to the size of nanoparticle, the distance between the nanoparticles, and the permittivity surrounding the nanoparticles. Since the size of Au-NPs and the distance between the Au-NPs are very similar in our system, permittivity (ϵ), an important factor which should be taken into account in our temperature-dependent direct current (DC) determination, will influence the difference of activation energy of nanocomposite films. Here the permittivity of **10**/Au-NPs, composed of Ru(II) dication and two PF_6^- counterions, is supposed to be much larger than that of **9**/Au-NPs. Moreover, in view of a larger spatial crowding effect of $[Ru(bpy)]^{2+}$ complex **10** in comparison with that of **9**, less molecules can serve as bridges to link Au-NPs under the same experimental condition, also leading to larger permittivity in the case of **10**/Au-NPs nanocomposite film. Since the charging energy of the nanoparticle, an important factor in determining the barriers to electron injection, heavily depends on the permittivity of the surroundings around the nanoparticles, the influence of the above-mentioned two factors in permittivity may facilitate electron hopping between Au-NPs in the case of **10**/Au-NPs nanocomposite film, thereby contributing to the decrease of the average activation energy.

As is known, transport mechanisms are determined by the easiest conduction paths between the drain and source electrodes. In general, bigger Au-NPs take more responsibility for the observed electron transportation due to their larger free-electron density, and defects of the films also have a significant impact on the global conductance.[29] However, in our experiments, Au-NPs and dithiols are in the same sizes (~3.3 and 1.89 nm) and only the statistically average current can be recorded by the $I-V$ monitor between the $1 \times 1\ \mu m^2$ gap area, wherein a large number of molecules and Au-NPs contribute to generation of the whole current. In this sense, it is possible for us to compare the temperature dependent $I-V$ characteristics and discuss the possible conduction mechanisms of films **9**/Au-NPs and **10**/Au-NPs when the parallel experiments are carried out even though well-oriented (or defect-free) arrangements cannot be achieved. In fact, the results obtained in this way show that, at least by integral conductance measurements, electron transport through individual molecules can be revealed, which depend on the electronic structures and conformation of the molecules and are comparable to those of our previously reported well-oriented junctions.

3. Conclusions

Organic semiconductors containing metal binding sites within their molecular backbones are of a general interest in organic material chemistry. To date, the chemistry of some thiol-substituted Ru(II) complexes[30] and Au-NPs containing Ru(II) complexes[31] has been investigated. However, studies of fine tuning the molecular structures and comparisons of their morphology and electric properties, especially using metal complexation with organic semiconductors that contain metal binding sites within their molecular backbones, are rarely involved.

In this paper, novel 3,8-bis(4-mercaptophenyl)-1,10-phenanthroline and its ruthenium(II) complex were synthesized, characterized, and used for fabricating self-assembled films with Au-NPs. Five 3,8-disubstituted 1,10-phenanthroline derivatives including four six-coordinate ruthenium(II) complexes were fully characterized including their structural description. The self-assembled nanocomposite films were produced by mixing the dithiol molecules (**9** or **10)** and *tert*-dodecanethiol-protected active Au-NPs via in situ thiol-to-thiol ligand exchange in the presence of two facing Au electrodes with a $1 \times 1\ \mu m^2$ gap, wherein dithiols-bridged Au-NPs were chemisorbed to the electrodes by means of Au−S-bonded contacts. SEM images exhibit that Ru(II) complex **10**-bridged Au-NPs are easier to aggregate into bigger particles than ligand **9**-bridged Au-NPs. The difference in morphology is supposed to originate from the molecular conformation, π-conjugated system, and charge status of **9** and **10**.

Temperature-dependent $I-V$ measurements and comparisons for junctions **9**/Au-NPs and **10**/Au-NPs were carried out in the temperature range of 7−300 K and in the voltage range from −4 to 4 V. Classical Arrhenius plots and their linear fits were performed to give the average activation energy in the 120−300 K and 0.5−4 V region before and after metal-ion complexation for these nanodevices (ΔE = 47 meV for **9**/Au-NPs and ΔE = 24 meV for **10**/Au-NPs). Good linearity in this region implied that thermionic excitation-induced hopping conductance should dominate the conduction mechanism for these nanodevices. The difference in conductivity and barriers to injection for junctions **9**/Au-

(29) (a) Daniel, M. C.; Astruc, D. *Chem. Rev.* **2004**, *104*, 293−346. (b) Schmid, G.; Simon, U. *Chem. Commun.* **2005**, 697−710.

(30) (a) Thompson, A. M. W. C.; Bardwell, D. A.; Jeffery, J. C.; Rees, L. H.; Ward, M. D. *J. Chem. Soc., Dalton Trans.* **1997**, 721−726. (b) Otsuki, J.; Kameda, H.; Tomihira, S.; Sakaguchi, H.; Takido, T. *Chem. Lett.* **2002**, *6*, 610−611. (c) Ohlsson, J.; Wolpher, H.; Hagfeldt, A.; Grennberg, H. *J. Photochem. Photobiol. A* **2002**, *148*, 41−48. (d) Tuccitto, N.; Torrisi, V.; Cavazzini, M.; Morotti, T.; Puntoriero, F.; Quici, S.; Campagna, S.; Licciardello, A. *ChemPhysChem* **2007**, *8*, 227−230.

(31) (a) Glomm, W. R.; Moses, S. J.; Brennaman, M. K.; Papanikolas, J. M.; Franzen, S. *J. Phys. Chem. B* **2005**, *109*, 804−810. (b) Mayer, C. R.; Dumas, E.; Mayer, C. R.; Michel, A.; Secheresse, F. *Chem. Commun.* **2006**, 4183−4185. (c) Wang, S.; Sim, W. S. *Langmuir* **2006**, *22*, 7861−7866. (d) Pramod, P.; Sudeep, P. K.; Thomas, K. G.; Kamat, P. V. *J. Phys. Chem. B* **2006**, *110*, 20737−20741. (e) Mayer, C. R.; Dumas, E.; Miomandre, F.; Meallet-Renault, R.; Warmont, F.; Vigneron, J.; Pansu, R.; Etcheberry, A.; Secheresse, F. *New J. Chem.* **2006**, *30*, 1628−1637.

NPs and **10**/Au-NPs is supposed to mainly come from introduction of the ruthenium(II) ion into the system. The former is somewhat related to the great band gap decrease from ligand **9** (4.149 eV) to $[Ru(bpy)_2]^{2+}$ complex **10** (2.614 eV) obtained by DFT calculations, wherein effects on the energy level quantization play an important role in the process of charge transfer within the self-assembled films. The latter is supposed to originate from the larger permittivity surrounding the nanoparticles **10** due to the different steric hindrance and charge status compared with that of **9**, given the very similar size of gold nanoparticles and the distance between the gold nanoparticles.

Further studies are in progress for fabricating self-assembled semiconducting films wherein other transition-metal ions and new conjugated terminal dithiols are introduced between two facing nanogap or microgap pair gold electrodes, investigating their morphology, electrical, and/or optical properties, quantum chemistry calculations, and elucidating possible conduction mechanisms for these molecular-based nanodevices.

4. Experimental Section

4.1. Materials and Measurements. All reagents and solvents were of analytical grade and used without further purification. The anhydrous solvents were drawn into a syringe under a flow of dry N_2 gas and directly transferred into the reaction flask to avoid contamination. *tert*-Dodecanethiol-protected active Au-NPs with an average size of 3.3 nm were prepared using a modified Brust method.[18,32] Gold electrodes with 1 μm gaps were prepared by a method described previously.[11a] Each 3 × 3 mm silicon chip was thoroughly washed with toluene, acetone, and methanol and cleaned in an oxygen plasma asher prior to SEM analysis. For preparation for self-assembled films with *tert*-dodecanethiol-ligated active Au-NPs in $CHCl_3$, the electrodes with 1 μm gaps were cleaned carefully in a CF_4 plasma and checked with an Olympus BX60M optical before use.

UV−vis spectra were recorded with a Shimadzu UV-3150 double-beam spectrophotometer using a Pyrex cell with a path length of 10 mm. Infrared spectra (FT-IR, 4000−400 cm^{-1}) were recorded using a Horiba FT-700 spectrophotometer. Analyses for carbon, hydrogen, and nitrogen were performed on a Perkin−Elmer 1400C analyzer. Cyclic voltammetry experiments were carried out with a BAS CV-50W voltammetric analyzer in a conventional three-electrode cell arrangement comprising a Pt coil counterelectrode, a Ag/Ag^+ (0.01 M, $TBAClO_4$ 0.1 M in CH_3CN) reference electrode, and a Pt working electrode (0.16 mm diameter). ^1H NMR spectra were collected on a Varian Unit 500 MHz spectrometer and a JEOL GSX 270 MHz spectrometer. ^{13}C NMR data were obtained at 67.8 MHz with a JEOL GSX spectrometer. DI-EI (70 eV) mass spectra were given by a Hitachi M80-B spectrometer. FAB-MS and time-of-flight mass spectra (TOF-MS) spectra were measured with a JEOL JMS-777V spectrometer. An OLYMPUS BX60M optical microscope was used to check all electrodes before determination of *I*−*V* curves. A Yanaco PLASMA ASHER LTA-102 instrument was used to clean all electrodes. Scanning electron microscope (SEM) images were collected with a JEOL JSM-6700F microscope with an acceleration voltage of 3 KV. Thermogravimetric analysis and differential thermal analysis (TGA-DTA) were recorded by a SHIMADZU simultaneous DTG-60A-type analyzer.

The *I*−*V* curves were collected with an Advantest R6245 2Channels Voltage Current Source Monitor interfaced to a microcomputer through a GPIB-SCSI board and NI-488.2 protocol. Data were acquired using a homemade procedure and Igor Pro 4.0 (Wavemetrics) software. The samples were mounted on the top of an antivibration table with a temperature-controlled cryogenic chamber (±0.005 °C). All measurements were carried out in high vacuum ($P < 2.0 \times 10^{-4}$ Pa at room temperature) formed by means of the turbomolecular pump, and the samples were cooled using liquid helium as the coolant (7−300 K). The positions of four Pt probes could be adjusted by *X*, *Y*, and *Z* directions in order to touch the Au electrodes. Short triaxial cables were used to connect the nanodevices and the *I*−*V* monitor in order to minimize the external noise.

4.2. X-ray Data Collection and Solution. All single-crystal samples were glue covered, mounted on glass fibers, and used for data collection on a Rigaku Mercury CCD area-detector at 100∼291 K using graphite monochromated Mo Kα radiation ($\lambda = 0.71073$ Å). The collected data were reduced using the program Crystalclear,[33] and empirical absorption corrections were done. The original data files generated by Crystalclear were transformed to SHELX-TL97 format by the TEXSAN program.[34] The crystal systems were determined by Laue symmetry, and the space groups were assigned on the basis of systematic absences using XPREP. The structures were solved by direct methods and refined by least-squares method on F_{obs}^2 using the SHELXTL-PC software package.[35] All non-H atoms were anisotropically refined, and all hydrogen atoms were inserted in the calculated positions, assigned fixed isotropic thermal parameters, and allowed to ride on their respective parent atoms. All calculations and molecular graphics were carried out with the SHELXTL PC program package. In the absence of significant anomalous scattering, Friedel equivalents were merged before the final refinement for **1**. Both of the PF_6^- counterions in **7** are disordered over two positions with different site occupancy factors at 0.851, 0.149 and 0.714, 0.286, respectively. One of two PF_6^- counterions in **8** is disordered over two positions with site occupancy factors of 0.532 and 0.468. A summary of the crystal data, experimental details, and refinement results for **1**, **3**, **4**, **7**, and **8** is listed in Table 1. Selected bond distances and bond angles involving the ruthenium ions and heteroatoms are given in Table 2, while versatile hydrogen-bonding interactions are tabulated in Table 4 (see Supporting Information).

4.3. Preparation of Compounds. 3,8-Dibromo-1,10-phenanthroline was prepared from 1,10-phenanthroline monohydrate by means of a method we described previously.[25]

3,8-Bis(4-methoxyphenyl)-1,10-phenanthroline (1). To the dry THF solution (80 mL) of 3,8-dibromo-1,10-phenanthroline (7.82 g, 23.1 mmol) and $NiCl_2$(dppp) (0.345 g, 0.64 mmol), the Grignard reagent prepared from 4-bromoanisole (7.85 mL, 62.5 mmol) and magnesium (2.12 g, 87.4 mmol) was added dropwise at 0 °C in nitrogen atmosphere. After stirring at room temperature for 18 h, the reaction mixture was treated with a saturated NH_4Cl aqueous solution and extracted with $CHCl_3$. The crude product was purified by a silica-gel column chromatography using $CHCl_3$ as the eluent and recrystallized from $CHCl_3$−hexane to give pure product as

(32) (a) Brust, M.; Walker, M.; Bethell, D.; Schiffrin, D. J.; Whyman, R. *Chem. Commun.* **1994**, 801−802. (b) Brust, M.; Fink, J.; Bethell, D.; Schiffrin, D.J.; Kiely, C. *Chem. Commun.* **1995**, 1655−1656.

(33) *Crystalclear*, Version 1.3; Molecular Structure Corp.: The Woodlands, TX, and Rigaku Corp.: Toyko, Japan, 2001.

(34) *TEXSAN*, Version 1.11; Molecular Structure Corp.: The Woodlands, TX, and Rigaku Corp.: Toyko, Japan, 2000.

(35) Sheldrick, G. M. *SHELXTL*, Version 6.10; Software Reference Manual; Bruker AXS, Inc.: Madison, WI, **2000**.

yellow crystalline solids in a yield of 40%. Mp 272−274 °C. ^{1}H NMR (270 MHz, $CDCl_3$, 298 K, TMS): (phen = 1,10-phenanthroline, bpy = 2,2′-bipyridine) δ 9.41 (d, J = 2.3 Hz, 2H, phen), 8.34 (d, J = 2.3 Hz, 2H, phen), 7.85 (s, 2H, phen), 7.70−7.77 (m, 4H, phenyl), 7.05−7.13 (m, 4H, phenyl), 3.90 (s, 6H, OCH_3). ^{13}C NMR (270 MHz, $CDCl_3$, 298 K, TMS): δ 160.0, 149.1, 144.5, 135.2, 132.5, 129.9, 128.6, 128.3, 127.0, 114.7, 55.4. Main FT-IR (KBr pellets, ν, cm^{-1}): 1606 (m), 1518 (m), 1432 (m), 1290 (m), 1250 (s), 1180 (m), 834 (m) cm^{-1}. Anal. Calcd for $C_{26}H_{20}N_2O_2$: C, 79.57; H, 5.14; N, 7.14. Found: C, 79.45; H, 5.13; N, 7.10. MS (EI, *m/z*): 392 (M^+), 377, 344, 286. UV−vis (λ max/ϵ (L·mol^{-1}·cm^{-1})) in methanol: 356 (6272), 287 (9045), 252 (7941), 228 (6199) nm. Single crystals of **1** suitable for X-ray diffraction determination were grown from the mixture of methanol/water (4:1, v/v) by slow evaporation in air at room temperature.

3,8-Bis(4-hydroxyphenyl)-1,10-phenanthroline (2). A mixture of **1** (2.37 g, 6.50 mmol) and pyridinium chloride (8.33 g, 72.0 mmol) was heated in a nitrogen atmosphere at 195 °C for 5 h with stirring. After cooling to the room temperature the mixture was treated with pure water, filtered, and washed with water until the filtrate become neutral and then washed with methanol. The solid product was dried under vacuum to give yellow crystals in a yield of 95%. Mp > 300 °C. ^{1}H NMR (270 MHz, acetone-d_6, 298 K, TMS): δ 9.37 (d, J = 1.5 Hz, 2H, phen), 8.58 (d, J = 5.0 Hz, 2H, phen), 8.01 (s, 2H, phen), 7.79−7.81 (m, 4H, phenyl), 7.05−7.07 (m, 4H, phenyl), 5.18 (s, 2H, OH). Main FT-IR (KBr pellets, ν, cm^{-1}): 3224 (br), 1608 (s), 1520 (s), 1436 (s), 1274 (s), 1236 (s), 1176 (s), 838 (s). Anal. Calcd for $C_{24}H_{16}N_2O_2$: C, 79.11; H, 4.43; N, 7.69. Found: C, 79.03; H, 4.59; N, 7.52. MS (EI, *m/z*): 365, 364 (M^+), 363, 272.

Bis(2,2′-bipyridine)(3,8-bis(4-methoxyphenyl)-1,10-phenanthroline)ruthenium(II) tetrafluoroborate (3). Complex **3** was synthesized by refluxing stoichiometric amounts of *cis*-bis(2,2′-bipyridine)dichlororuthenium(II) hydrate (0.484 g, 1.0 mmol) and **1** (0.364 g, 1.0 mmol) in 100 mL of methanol, and then the mixture was treated in situ anion exchange reaction by adding excess $NaBF_4$ aqueous solution in order to precipitate the complex. ^{1}H NMR (500 MHz, acetone-d_6, 298 K, TMS): δ 8.99 (d, J = 1.70 Hz, 2H, phen), 8.88 (d, 2H, J = 8.30 Hz, bpy), 8.81 (d, 2H, J = 8.05 Hz, bpy), 8.43 (d, 2H, J = 1.95 Hz, phen), 8.41 (s, 2H, phen), 8.30−8.28 (m, 2H, bpy), 8.26 (d, 2H, J = 5.15 Hz, bpy), 8.15 (d, 2H, J = 7.80 Hz, bpy), 8.13−8.10 (m, 2H, bpy), 7.68−7.66 (m, 2H, bpy), 7.58 (d, 4H, J = 8.80 Hz, phenyl), 7.42−7.39 (m, 2H, bpy), 7.04 (d, 4H, J = 8.80 Hz, phenyl), 3.84 (s, 6H, OCH_3). Main FT-IR (KBr pellets, ν, cm^{-1}): 3422 (br), 2925 (w), 1655 (w), 1605 (s), 1561 (m), 1519 (s), 1465 (s), 1439 (s), 1381 (m), 1291 (m), 1253 (s), 1183 (s), 1122 (s), 1084 (vs), 1059 (vs), 837 (m), 770 (m). Anal. Calcd for $C_{46}H_{36}N_6O_2$ Ru·B_2F_8: C, 56.41; H, 3.70; N, 8.58. Found: C, 56.45; H, 3.87; N, 8.62. MS (FAB, *m/z*): 893 (M^+ − BF_4). UV−vis (λ max/ϵ (L·mol^{-1}·cm^{-1})) in methanol 451 (1439), 364 (4265), 288 (8793), 255 (5778), 234 (4356) nm; in the solid state 462, 389, 296, 258 nm. Single crystals of **3** suitable for X-ray diffraction determination were grown from the mixtures of ethanol/water (2:1, v/v) by slow evaporation in air at room temperature.

Bis(2,2′-bipyridine)(3,8-bis(4-ethoxyphenyl)-1,10-phenanthroline)ruthenium(II) hexafluorophosphorate (4). The preparation method was identical to **3** except that excess NH_4PF_6 aqueous solution was utilized to precipitate the complex. ^{1}H NMR (500 MHz, acetone-d_6, 298 K, TMS): δ 8.98 (d, 2H, J = 1.70 Hz, phen), 8.87 (d, 2H, J = 8.05 Hz, bpy), 8.80 (d, 2H, J = 8.05 Hz, bpy), 8.43 (d, 2H, J = 1.95 Hz, phen), 8.40 (s, 2H, phen), 8.30−8.28 (m, 2H, bpy), 8.26 (d, 2H, J = 5.60 Hz, bpy), 8.15 (d, 2H, J = 5.15 Hz, bpy), 8.13−8.10 (m, 2H, bpy), 7.68−7.65 (m, 2H, bpy), 7.56 (d, 4H, J = 8.75 Hz, phenyl), 7.42−7.39 (m, 2H, bpy), 7.02 (d, 4H, J = 8.75 Hz, phenyl), 4.12−4.07 (m, 4H, CH_2), 1.37 (t, 6H, Me). Main FT-IR (KBr pellets, ν, cm^{-1}): 3436 (br), 3081 (w), 2978 (w), 2928 (m), 1606 (s), 1518 (s), 1467 (s), 1437 (s), 1392 (m), 1289 (m), 1250 (s), 1183 (s), 1041 (m), 843 (vs), 764 (s), 557 (s). Anal. Calcd for $C_{48}H_{40}N_6O_2$ Ru·P_2F_{12}: C, 51.30; H, 3.59; N, 7.48. Found: C, 51.41; H, 3.70; N, 7.53. MS (FAB, *m/z*): 979 (M^+ − PF_6). UV−vis (λ max/ϵ (L·mol^{-1}·cm^{-1})) in methanol: 451 (1509), 365 (4100), 288 (8728), 255 (5943), 234 (4660) nm, in the solid state 458, 383, 295, 258 nm. Single crystals of **4** suitable for X-ray diffraction determination were grown from mixtures of ethanol/acetone (2:1, v/v) by slow evaporation in air at room temperature.

3,8-Bis(4-(*N*,*N*′-dimethylthiocarbamoyl)oxyphenyl)-1,10-phenanthroline (5). A mixture of **2** (2.0 g, 5.5 mmol), *N*,*N*-dimethylthiocarbamoyl chloride (4.1 g, 33 mmol), and 4-*N*,*N*-dimethylaminopyridine (0.18 g, 1.5 mmol) in dry pyridine (60 mL) was heated at 80 °C for 18 h under N_2. After the solvent was removed under a vacuum, the product was extracted with $CHCl_3$ and purified by silica-gel column chromatography using a mixture of $CHCl_3$/ethanol (99:1) as the eluent; the product was obtained as yellow solids in a yield of 51%. Mp > 300 °C. ^{1}H NMR (270 MHz, $CDCl_3$, 298 K, TMS): δ 9.45 (d, J = 2.1 Hz, 2H, phen), 8.40 (d, J = 2.1 Hz, 2H, phen), 7.87 (s, 2H, phen), 7.76−7.85 (m, 4H, phenyl), 7.2−37.32 (m, 4H, phenyl), 3.50 (s, 6H, NCH_3), 3.40 (s, 6H, NCH_3). ^{13}C NMR (270 MHz, $CDCl_3$, 298 K, TMS): δ 187.5, 154.2, 149.4, 145.0, 135.2, 134.9, 133.3, 128.4, 128.3, 127.1, 123.6, 43.3, 38.8. Main FT-IR (KBr pellets, ν, cm^{-1}): 3036 (m), 2956 (m), 1538 (m), 1512 (m), 1434 (s), 1394 (m), 1286 (m), 1214 (m), 1172 (m), 1130 (m), 842 (m), 740 (m). Anal. Calcd for $C_{30}H_{26}N_4O_2S_2$: C, 66.89; H, 4.86; N, 10.40. Found: C, 66.82; H, 4.80; N, 10.51. MS (EI, *m/z*): 538 (M^+), 88, 72.

3,8-Bis(4-(*N*,*N*′-dimethylcarbamoyl)thiophenyl)-1,10-phenanthroline (6). Compound **5** (0.48 g, 0.89 mmol) was heated under an argon atmosphere in a glass tube oven at 300 °C for 6 h. The resultant solid was dissolved in $CHCl_3$, filtered through celite, and purified by silica-gel column chromatography using $CHCl_3$ as the eluent. The product was obtained as yellow crystals in a yield of 89%. Mp > 300 °C. ^{1}H NMR (270 MHz, $CDCl_3$, 298 K, TMS): δ 9.44 (d, J = 2.3 Hz, 2H, phen), 8.41 (d, J = 2.3 Hz, 2H, phen), 7.90 (s, 2H, phen), 7.78−7.82 (m, 4H, phenyl), 7.66−7.70 (m, 4H, phenyl), 3.00−3.10 (br d, 12H, $N(CH_3)_2$). ^{13}C NMR (270 MHz, $CDCl_3$, 298 K, TMS): δ 166.5, 149.5, 145.3, 138.4, 136.4, 135.1, 133.5, 129.3, 128.5, 128.0, 127.2, 37.0. Main FT-IR (KBr pellets, ν, cm^{-1}): 2944 (w), 1662 (s), 1434 (m), 1362 (m), 1090 (s), 832 (w), 742 (w). MS (EI, *m/z*): 538 (M^+), 88, 72. UV−vis (λmax/ϵ (L·mol^{-1}·cm^{-1})) in methanol: 334 (4039), 278 (9987), 204 (13 032) nm.

Bis(1,10-phenanthroline)(3,8-bis(4-(*N*,*N*′-dimethylthiocarbamoyl)oxyphenyl)-1,10-phenanthroline)ruthenium(II) Hexafluorophosphorate (7). Complex 7 was prepared via a method similar to that of 8 except that *cis*-bis(1,10-phenanthroline)dichlororuthenium(II) was used to replace *cis*-bis(2,2′-bipyridine)dichlororuthenium(II) hydrate. Yield 81%. Mp > 300 °C. ^{1}H NMR (270 MHz, acetone-d_6, 298 K, TMS): δ 9.06 (d, J = 1.5 Hz, 2H, phen), 8.79 (d, J = 1.0 Hz, 2H, phen), 8.77 (d, J = 1.0 Hz, 2H, phen), 8.63 (d, J = 4.5 Hz, 2H, phen), 8.61 (d, J = 2.0 Hz, 2H, phen), 8.50 (s, 2H, phen), 8.46 (d, J = 5.0 Hz, 2H, phen), 8.37 (s, 4H, phen), 7.83 (d, J = 5.0 Hz, 2H, phen), 7.82 (d, J = 5.0 Hz, 2H, phen), 7.47−7.53 (dd, J = 8.5 and 8.5 Hz, 8H, phenyl), 3.56−3.41 (br d, 12H, $N(CH_3)_2$). Main FT-IR (KBr pellets, ν, cm^{-1}): 1656 (m), 1543 (m), 1510 (m), 1429 (m), 1397 (m), 1285(m), 1214 (s), 1174 (s), 1130 (m), 839 (s), 722 (w), 558 (m). Anal. Calcd for $C_{54}H_{42}N_8O_2S_2$-

$Ru{\cdot}P_2F_{12}$: C, 50.27; H, 3.28; N, 8.69. Found: C, 50.43; H, 3.41; N, 8.78. MS (FAB, *m/z*): 1145 ($M^+ - PF_6$). UV−vis (λ max/ϵ ($L{\cdot}mol^{-1}{\cdot}cm^{-1}$)) in methanol: 446 (1537), 347 (3726), 263 (10 912), 204 (18 070) nm. Single-crystal sample of ruthenium(II) complex **7** suitable for X-ray diffraction determination was grown from a mixed solution of CH_3CN/MeOH/H_2O (2:4:1, v/v) by slow evaporation in air at room temperature.

Bis(2,2′-bipyridine)(3,8-bis(4-(*N*,*N*′-dimethylcarbamoyl)thiophenyl)-1,10-phenanthroline)ruthenium(II) Hexafluorophosphorate (8). To a dry-DMF (6 mL) solution of **6** (0.32 g, 0.59 mmol) heated at 60 °C was added a dry-DMF (8 mL) solution of *cis*-bis(2,2′-bipyridine)dichlororuthenium(II) hydrate (0.24 g, 0.50 mmol). The solution was heated to 140 °C and stirred for 16 h. When the reaction was completed, the solvent was removed in vacuo and dissolved in water. Saturated aqueous solution (5 mL) of NH_4PF_6 was added, and the precipitates were collected by filtration. The solids were dried in vacuo to give vermilion powder in a yield of 91%. Mp > 300 °C. ^{1}H NMR (270 MHz, acetone-d_6, 298 K, TMS): δ 9.11 (d, J = 2.0 Hz, 2H, phen), 8.86 (br d, J = 7.6 Hz, 2H, bpy), 8.79 (br d, J = 7.6 Hz, 2H, bpy), 8.58 (d, J = 2.0 Hz, 2H, phen), 8.50 (s, 2H, phen), 8.24−8.30 (m, 4H, bpy), 8.11−8.16 (m, 4H, bpy), 7.63−7.72 (m, 6H, phenyl + bpy), 7.54−7.60 (m, 4H, phenyl), 7.40 (ddd, J = 7.1, 5.6, 1.0 Hz, 2H, bpy), 3.00−3.10 (br d, 12H, $N(CH_3)_2$). ^{13}C NMR (270 MHz, acetone-d_6, 298 K, TMS): δ 165.93, 159.05, 153.72, 152.28, 147.65, 139.46, 139.37, 139.28, 137.50, 137.23, 135.88, 132.49, 132.37, 130.24, 129.14, 129.04, 125.83, 37.39. Main FT-IR (KBr pellets, ν, cm^{-1}): 1666 (s), 1468 (m), 1448 (m), 1436 (m), 1366 (m), 1092 (m), 844 (s), 766 (m), 560 (s). Anal. Calcd for $C_{50}H_{42}N_8O_2S_2Ru{\cdot}P_2F_{12}$: C, 48.35; H, 3.41; N, 9.02. Found: C, 48.55; H, 3.59; N, 8.74. MS (FAB, *m/z*): 1097 ($M^+ - PF_6$), 952 ($M^+ - 2PF_6$). UV−vis (λ max/ϵ ($L{\cdot}mol^{-1}{\cdot}cm^{-1}$)) in methanol: 451 (1482), 346 (4993), 287 (10 536), 204 (17 583) nm. A single-crystal sample of ruthenium(II) complex **7** suitable for X-ray diffraction determination was grown from a mixed solution of chloroform and acetone in a ratio of 2:1 (v/v) by slow evaporation in air at room temperature.

3,8-Bis(4-mercaptophenyl)-1,10-phenanthroline (9). A solution of compound **6** (1.082 g, 2.01 mmol) and KOH (1.94 g, 85%, 29.4 mmol) in 24 mL of THF/EtOH (1:2, v/v) was heated at 70 °C under a nitrogen atmosphere for 18 h. After the reaction was completed, the solvent was removed by a rotary evaporator. The residue was acidified by 10% HCl aqueous solution, and the precipitated yellow solids were filtered, washed with pure water and a small amount of methanol, and dried in vacuo to give **12** in a yield of 84%. Mp > 300 °C. ^{1}H NMR (500 MHz, $CDCl_3$, 298 K, TMS): δ 9.43 (d, J = 1.5 Hz, 2H, phen), 8.43 (d, J = 3.5 Hz, 2H, phen), 7.92 (s, 2H, phen), 7.69−7.75 (m, 4H, phenyl), 7.51−7.67 (m, 4H, phenyl), 3.56 (s, 2H, thiol). Main FT-IR (KBr pellets, ν, cm^{-1}): 3048 (w), 1594 (s), 1472 (m), 1288 (m), 1106 (s), 830 (s). Anal. Calcd for $C_{24}H_{16}N_2S_2$: C, 72.70; H, 4.07; N, 7.06. Found: C, 72.59; H, 4.28; N, 7.12. MS (EI, *m/z*): 396 (M^+), 363, 280.

Bis(2,2′-bipyridine)(3,8-bis(4-mercaptophenyl)-1,10-phenanthroline)ruthenium(II) Hexafluorophosphorate (10). A solution of ruthenium(II) complex **8** (0.25 g, 0.19 mmol) and KOH (0.26 g, 4.01 mmol) in 20 mL of methanol was heated at 70 °C under a nitrogen atmosphere for 18 h. After the reaction was completed, the solvent was removed in a vacuum, the residue was dissolved in water, and the solution was acidified by 10% HCl aqueous solution. Saturated aqueous solution (5 mL) of NH_4PF_6 was added, and the precipitated brown solids were collected, washed with water, and dried in vacuo to give the brown product in a yield of 84%. Mp > 300 °C. ^{1}H NMR (400 MHz, acetone-d_6, 298 K, TMS): δ 9.03 (d, J = 2.0 Hz, 2H, phen), 8.86 (br d, J = 7.8 Hz, 2H, bpy), 8.79 (br d, J = 7.8 Hz, 2H, bpy), 8.47 (d, J = 2.0 Hz, 2H, phen), 8.44 (s, 2H, phen), 8.25−8.30 (m, 4H, bpy), 8.14 (ddd, J = 7.1, 6.4, 1.5 Hz, 2H, bpy), 8.09 (br d, J = 4.9 Hz, 2H, bpy), 7.67 (ddd, J = 6.3, 5.4, 1.0 Hz, 2H, bpy), 7.49−7.54 (m, 4H, phenyl), 7.36−7.44 (m, 6H, phenyl + bpy), 3.69 (s, 2H, thiol). ^{13}C NMR (400 MHz, acetone-d_6, 298 K, TMS): δ 159.08, 158.61, 153.74, 151.86, 147.71, 139.45, 139.28, 133.51, 135.14, 136.18, 132.33, 130.47, 130.14, 129.47, 129.14, 129.04, 125.81. ^{19}F NMR (270 MHz, acetone-d_6): δ −70.23 (s, 6F), −73.01 (s, 6F). Main FT-IR (KBr pellets, ν, cm^{-1}): 1601 (m), 1446 (m), 1435 (m), 843 (s), 764 (m), 557 (m). Anal. Calcd for $C_{44}H_{32}N_6S_2Ru{\cdot}P_2F_{12}$: C, 48.05; H, 2.93; N, 7.64. Found: C, 48.01; H, 2.99; N, 7.72. MS (FAB, *m/z*): 1097 ($M^+ - 3$), 955 ($M^+ - PF_6$), 809 ($M^+ - 2PF_6 - 1$).

Preparation of Self-Assembled Film Consisting of 9- and 10-Bridged Au-NPs on 1 μm Gap Au Electrodes. The nanojunctions were fabricated by the self-assembly method according to a similar method we described before.[11] Freshly oxygen plasma cleaned gold electrode pairs with a 1 × 1 μm^2 gap (four pairs in each chip) were immersed in the DMF solutions of 9 and 10 (0.05, 0.1, or 0.5 mmol/L) for 30 min, respectively, and then the chloroform solution of *tert*-dodecanethiol-protected active Au-NPs (0.05, 0.1, or 0.5 mmol/L) was added. The mixtures were covered and kept standing for 30 h at room temperature in a glovebox. The electrodes were then taken out, washed thoroughly with DMF and chloroform in order to remove excess Au-NPs and dithiols, and dried in a vacuum.

Acknowledgment. This work was supported by a Grant-in-Aid for Scientific Research (Nos. 15201028 and 14654135) and for Key-Technology, 'Atomic Switch Programmed Device' from the Ministry of Culture, Education, Science Sports, and Technology of Japan. W.H. acknowledges the Major State Basic Research Development Programs (Nos. 2007CB925101 and 2006CB806104), the National Natural Science Foundation of China (No. 20721002), and the Scientific Research Foundation for the Returned Overseas Chinese Scholars, State Education Ministry for financial aid. The authors would also like to thank H. Tanemura for help in synthesis.

Supporting Information Available: Crystallographic information files (CIFs) for all five structures, hydrogen-bonding interactions, crystal-packing views, and additional SEM images of nanocomposite films before and after self-assembly. This material is available free of charge via the Internet at http://pubs.acs.org. In addition, CCDC reference Nos. 298745−298749 contain the supplementary crystallographic data presented in this paper (corresponding to **1**, **3**, **4**, **7**, and **8**). The data can also be obtained free of charge at www.ccdc.cam.ac.uk/conts/retrieving.html [or from the Cambridge Crystallographic Data Centre, 12, Union Road, Cambridge CB2 1EZ, UK; Fax: +44-1223/336-033; E-mail: deposit@ccdc.cam.ac.uk].

IC701295Q